Journal of Systems Engineering and Electronics
Vol. 30, No. 2, April 2019, pp.270 – 277

Modified version of three-component model-based decomposition for polarimetric SAR data

ZHANG Shuang[1,*], YU Xiangchuan[2], and WANG Lu[1]

1. School of Automation and Information Engineering, Xi'an University of Technology, Xi'an 710048, China;
2. Caltta Technologies Co., Ltd., Beijing 100191, China

Abstract: A new hybrid Freeman/eigenvalue decomposition based on the orientation angle compensation and the various extended volume models for polarimetric synthetic aperture radar (PolSAR) data are presented. There are three steps in the novel version of the three-component model-based decomposition. Firstly, two special unitary transform matrices are applied on the coherency matrix for deorientation to decrease the correlation between the co-polarized term and the cross-polarized term. Secondly, two new conditions are proposed to distinguish the man-made structures and the nature media after the orientation angle compensation. Finally, in order to adapt to the scattering properties of different media, five different volume scattering models are used to decompose the coherency matrix. These new conditions pre-resolves man-made structures, which is beneficial to the subsequent selection of a more suitable volume scattering model. Fully PolSAR data on San Francisco are used in the experiments to prove the efficiency of the proposed hybrid Freeman/eigenvalue decomposition.

Keywords: polarimetric synthetic aperture radar (PolSAR), radar polarimetry hybrid Freeman/eigenvalue decomposition, scattering model.

DOI: 10.21629/JSEE.2019.02.06

1. Introduction

The target decomposition theorem is an important and advanced tool for polarimetric synthetic aperture radar (PolSAR) data [1,2] and it has been applied successfully to many areas of PolSAR data, such as disaster monitoring [3 – 5], crop monitoring [6,7], target detection [8,9] and classification [10 – 15].

There are two major advantages [1,2]. Firstly, the target decomposition does not depend on the statistical distribution of PolSAR data, thus it is not necessary to set that PolSAR data obey a certain statistical distribution, and then complex calculations and cumulative errors are avoided. Secondly, the parameters derived from the target decomposition usually empress the physical meaning of PolSAR objects. Therefore, many decomposition techniques are proposed in the past two decades.

Target decomposition methods are divided into two groups, i.e., the coherent target decomposition and the incoherent target decomposition. Contrast to the measured scattering matrix for the coherent target decomposition, the second-order statistics such as the coherency matrix or the covariance matrix are used for the incoherent target decomposition because of the anti-noise performance.

Incoherent target decomposition techniques can be categorized into two representative groups, i.e., the model-based decomposition approaches introduced by Freeman et al. [16] and the eigenvalue-based target decomposition approaches firstly introduced by Cloude et al. [17]. Among various model-based decomposition approaches, the Freeman-Durden decomposition (FDD) [16] interprets the measured covariance matrix in terms of three independent scattering components, i.e., surface scattering, double-bounce scattering and volume scattering.

After the initial work of Freeman and Durden, many researchers pay considerable attention to the model-based decompositions. In the FDD, because the cross-polarized term only exists in the volume scattering model, the volume scattering power may be overestimated while the total power is fixed, thus the surface scattering and double-bounce scattering power may be too small or even negative, which is the key problem of the FDD [16, 18]. There are two ways to solve this negative power problem. The first one is to propose more suitable scattering models, especially the volume scattering model [19 – 29], or to add a new scattering component to share the volume scattering power [18,30,31], such as the helix scattering component. The second one is the orientation angle compensation

Manuscript received May 16, 2018.
*Corresponding author.
This work was supported by the National Natural Science Foundation of China (41704118; 11747032), the Natural Science Basic Research Plan in Shaanxi Province of China (2017JQ6065; 2017JQ4017), and the Special Scientific Research Project of Shaanxi Provincial Education Department (18JK0549).

(OAC) on the coherency matrix [32 – 36]. The OAC decreases the cross-polarized term, which leads to the smaller volume scattering power, the nonnegative surface scattering power and the double-bounce scattering power. Arii et al. [20] and An et al. [35] also used the power constraint to solve the negative power problem. In their methods, if the volume scattering power is bigger than the total power, it is set to be equal to the total power, at the mean time the negative surface scattering power and the negative double-bounce scattering power are set to be zero. Cloude [37] proposed a modified decomposition that the surface scattering model was orthogonal with the double-bounce scattering model. This method combines the Freeman-Durden decomposition with the eigenvalue-based decomposition together. To solve the negative power problem, the OAC on the coherency matrix is also used [38], which is named as Freeman/eigenvalue decomposition.

In this paper, a novel Freeman/eigenvalue decomposition is improved from three aspects. Firstly, two kinds of the OAC are used to the coherency matrix to reduce the value of the cross-polarized term. Secondly, five different volume scattering models are used with a new discriminant to make sure that the scattering powers are more consistent with the actual targets. Finally, the power constraint is also used to avoid the negative powers. The effectiveness of the new decomposition algorithm is verified by the real PolSAR data.

2. OAC and scattering models

2.1 Coherency matrix and OAC

For the monostatic fully PolSAR system with {H, V} basis, we can obtain the Sinclear matrix as follows:

$$\boldsymbol{S} = \begin{bmatrix} S_{HH} & S_{HV} \\ S_{VH} & S_{VV} \end{bmatrix}. \tag{1}$$

If the PolSAR targets obey the reciprocal condition (i.e., $S_{HV} = S_{VH}$), the single look PolSAR data can be expressed in the Pauli scattering vector:

$$\boldsymbol{k}_p = \frac{1}{\sqrt{2}} \begin{bmatrix} S_{HH} + S_{VV} \\ S_{HH} + S_{VV} \\ 2S_{HV} \end{bmatrix}. \tag{2}$$

The multi-look PolSAR data can be expressed by a 3×3 coherency matrix:

$$\langle [T] \rangle = \langle \boldsymbol{k}_p * \boldsymbol{k}_p^{\mathrm{H}} \rangle = \begin{bmatrix} T_{11} & T_{12} & T_{13} \\ T_{12}^* & T_{22} & T_{23} \\ T_{13}^* & T_{23}^* & T_{33} \end{bmatrix} \tag{3}$$

where $\langle \ \rangle$ denotes the multi-look processor, and the superscript H denotes the conjugate transposition processor. The coherency matrix is a Hermite matrix.

In order to decrease the cross-polarized term T_{33}, the coherency matrix is rotated by the unit matrix $\boldsymbol{R}(\theta)$ [35], where θ is the angle of the rotation, i.e. the OAC. The elements in $\boldsymbol{R}(\theta)$ are all real values.

$$\boldsymbol{R}(\theta) = \begin{bmatrix} 1 & 0 & 0 \\ 0 & \cos(2\theta) & \sin(2\theta) \\ 0 & -\sin(2\theta) & \cos(2\theta) \end{bmatrix} \tag{4}$$

The coherency matrix after the OAC $\langle [T(\theta)] \rangle$ is shown as follows:

$$\langle [T(\theta)] \rangle = \boldsymbol{R}(\theta) \langle [T] \rangle \boldsymbol{R}^{-1}(\theta) = \begin{bmatrix} T_{11}(\theta) & T_{12}(\theta) & T_{13}(\theta) \\ T_{12}^*(\theta) & T_{22}(\theta) & T_{23}(\theta) \\ T_{13}^*(\theta) & T_{23}^*(\theta) & T_{33}(\theta) \end{bmatrix}. \tag{5}$$

The elements of $\langle [T(\theta)] \rangle$ are shown as follows:

$$\begin{cases} T_{11}(\theta) = T_{11} \\ T_{12}(\theta) = T_{12}\cos(2\theta) + T_{13}\sin(2\theta) \\ T_{13}(\theta) = -T_{12}\sin(2\theta) + T_{13}\cos(2\theta) \\ T_{23}(\theta) = \mathrm{jIm}(T_{23}) \\ T_{22}(\theta) = T_{22}\cos^2(2\theta) + T_{33}\sin^2(2\theta) + \\ \qquad \mathrm{Re}(T_{23})\sin(4\theta) \\ T_{33}(\theta) = T_{33}\cos^2(2\theta) + T_{22}\sin^2(2\theta) - \\ \qquad \mathrm{Re}(T_{23})\sin(4\theta) \end{cases}. \tag{6}$$

From (6), the real part of $T_{23}(\theta)$ in the coherency matrix after the OAC is equal to zero. By minimizing the cross-polarized term $T_{33}(\theta)$, the rotation angle θ is solved:

$$\theta = \frac{1}{4}\arctan\left(\frac{2\mathrm{Re}(T_{23})}{T_{22} - T_{33}}\right) + \frac{n\pi}{4}, \quad n = 0, \pm 1 \tag{7}$$

where $\mathrm{Re}(T_{23})$ is the real part of T_{23}. The total power and $T_{11}(\theta)$ are fixed, thus $T_{33}(\theta)$ becomes smaller and $T_{22}(\theta)$ becomes larger. The power transfers from $T_{33}(\theta)$ to $T_{22}(\theta)$.

The second rotation matrix is a unit complex matrix (in (8)), which usually is carried on $T(\theta)$, and the coherency matrix after the complex matrix rotation is given by (9).

$$\boldsymbol{U}(\varphi) = \begin{bmatrix} 1 & 0 & 0 \\ 0 & \cos(2\varphi) & \mathrm{j}\sin(2\varphi) \\ 0 & -\mathrm{j}\sin(2\varphi) & \cos(2\varphi) \end{bmatrix} \tag{8}$$

$$\langle [T(\varphi)] \rangle = \boldsymbol{U}(\varphi) \langle [T(\theta)] \rangle \boldsymbol{U}^{-1}(\varphi) = \begin{bmatrix} T_{11}(\varphi) & T_{12}(\varphi) & T_{13}(\varphi) \\ T_{12}^*(\varphi) & T_{22}(\varphi) & T_{23}(\varphi) \\ T_{13}^*(\varphi) & T_{23}^*(\varphi) & T_{33}(\varphi) \end{bmatrix} \tag{9}$$

In the same way, each element in the coherency matrix after the complex rotation and the rotation angle φ is shown as follows:

$$\begin{cases} T_{11}(\varphi) = T_{11} \\ T_{12}(\varphi) = T_{12}(\theta)\cos(2\varphi) + T_{13}(\theta)\sin(2\varphi) \\ T_{13}(\varphi) = -T_{12}(\theta)\sin(2\varphi) + T_{13}(\theta)\cos(2\varphi) \\ T_{23}(\varphi) = 0 \\ T_{22}(\varphi) = T_{22}(\theta)\cos^2(2\varphi) + T_{33}(\theta)\sin^2(2\varphi) + \\ \qquad \mathrm{Im}(T_{23}(\theta))\sin(4\varphi) \\ T_{33}(\theta) = T_{33}(\theta)\cos^2(2\varphi) + T_{22}(\theta)\sin^2(2\varphi) - \\ \qquad \mathrm{Re}(T_{23}(\theta))\sin(4\varphi) \end{cases} \tag{10}$$

$$\varphi = \frac{1}{4}\arctan\left(\frac{2\mathrm{Im}(T_{23}(\theta))}{T_{22}(\theta) - T_{33}(\theta)}\right) + \frac{m\pi}{4}, \quad m = 0, \pm 1. \tag{11}$$

After two rotations, the cross-polarized term T_{33} is reduced, and then the negative scattering powers became less even disappeared. The detailed decomposition algorithm will be demonstrated in the next section.

2.2 Scattering models

The rotated coherency matrix can be expanded into three sub-matrices [16]:

$$\langle [T] \rangle = m_s \boldsymbol{T}_s + m_d \boldsymbol{T}_d + m_v \boldsymbol{T}_v \tag{12}$$

where $\boldsymbol{T}_s$, $\boldsymbol{T}_d$ and $\boldsymbol{T}_v$ are the surface scattering model, the double-bounce scattering model and the volume scattering model, respectively. m_s, m_d and m_v represent the corresponding surface scattering power, the double-bounce scattering power and the volume scattering power, respectively.

The next part reviews the surface scattering model, the double-bounce scattering model, various volume scattering models and the Freeman/eigenvalue decomposition [38].

2.2.1 Surface scattering model

The surface scattering model implies the odd-bounce scattering echo from slightly rough surfaces. The Sinclair matrix for the surface scattering model is shown as follows:

$$\boldsymbol{S}_s = \begin{bmatrix} R_H & 0 \\ 0 & R_V \end{bmatrix} \tag{13}$$

where R_h and R_V are the reflection coefficients from horizontally and vertically polarized waves. The cross-polarized term is negligible.

The coherency matrix for the surface scattering model is shown as follows:

$$\boldsymbol{T}_s = \frac{1}{|\beta|^2 + 1}\begin{bmatrix} 1 & \beta^* & 0 \\ \beta & |\beta|^2 & 0 \\ 0 & 0 & 0 \end{bmatrix} \tag{14}$$

where $\beta = \dfrac{R_H - R_V}{R_H + R_V}$, and $0 < \beta < 1$. The coefficient $\dfrac{1}{|\beta|^2 + 1}$ before the matrix is used to ensure that the total power of $\boldsymbol{T}_s$ is equal to 1.

2.2.2 Double-bounce scattering model

The double-bounce scattering usually occurs in the dihedral structure, e.g., the ground-building wall reflector, the ground-trunk reflector. The echo is received after two reflections, and expressed by a scattering matrix shown as follows:

$$\boldsymbol{S}_d = \begin{bmatrix} R_{TH}R_{GH} & 0 \\ 0 & R_{TV}R_{GV} \end{bmatrix}. \tag{15}$$

The corresponding coherency matrix for the double-bounce scattering model is defined as follows:

$$\boldsymbol{T}_d = \frac{1}{|\alpha|^2 + 1}\begin{bmatrix} 1 & \alpha^* & 0 \\ \alpha & |\alpha|^2 & 0 \\ 0 & 0 & 0 \end{bmatrix} \tag{16}$$

where α is a complex value with $|\alpha| < 1$, and the real part of α is negative. The total power of $\boldsymbol{T}_d$ is also equal to 1. The cross-polarized term is equal to 0.

2.2.3 Volume scattering model

The volume scattering can be modeled by a cloud of the oriented thin dipole, and the scattering matrix can be expressed as follows:

$$\boldsymbol{S}_{v1} = \begin{bmatrix} 1 & 0 \\ 0 & 1 \end{bmatrix}. \tag{17}$$

Via the integration with a uniform distribution probability density function $p(\theta)$ for the orientation angle of the thin dipole, the coherency matrix for the volume scattering model is expressed as follows:

$$\boldsymbol{T}_{v1} = \frac{1}{4}\begin{bmatrix} 2 & 0 & 0 \\ 0 & 1 & 0 \\ 0 & 0 & 1 \end{bmatrix}. \tag{18}$$

$\boldsymbol{T}_{v1}$ is the original volume scattering model, which is suitable for the uniform distribution targets, such as the forest with the thick crown canopy. Because the orientation angle of the received echo is likely to be the uniform distribution in $[0, \pi]$, thus the volume scattering can be modeled as (18). However, the ideal hypothesis does not hold all the time, and several modified visions are developed.

If the volume scattering is modeled by a cloud of the horizontal thin dipole, the scattering matrix can be expressed as follows:

$$\boldsymbol{S}_{v2} = \begin{bmatrix} 1 & 0 \\ 0 & 0 \end{bmatrix}. \tag{19}$$

Accordingly, the coherency matrix for the volume scattering model can be expressed as follows:

$$\boldsymbol{T}_{v2} = \frac{1}{30}\begin{bmatrix} 15 & -5 & 0 \\ -5 & 7 & 0 \\ 0 & 0 & 8 \end{bmatrix}. \tag{20}$$

In a similar way, the scattering matrix modeled by a cloud of the vertical dipole can be expressed as (21), and the coherency matrix can be expressed as (22).

$$\boldsymbol{S}_{v3} = \begin{bmatrix} 0 & 0 \\ 0 & 1 \end{bmatrix} \tag{21}$$

$$\boldsymbol{T}_{v3} = \frac{1}{30}\begin{bmatrix} 15 & 5 & 0 \\ 5 & 7 & 0 \\ 0 & 0 & 8 \end{bmatrix} \tag{22}$$

In $\boldsymbol{T}_{v1}$, the two co-polarized terms T_{11} and T_{22} are mutually independent, i.e., $T_{12} = 0$. In contrast, $T_{12} = -5$ and $T_{12} = 5$ in T_{v2} and T_{v3}, respectively, indicate that the two co-polarized terms are related. Therefore, in the real PolSAR data, the three volume scattering models are distinguished by the co-polarized ratio.

Another case for the homogeneous targets should be discussed. When the targets are totally random scattering, the entropy of the measured coherency matrix is one [35,39], thus the volume scattering is expressed as follows:

$$\boldsymbol{T}_{v4} = \frac{1}{3}\begin{bmatrix} 1 & 0 & 0 \\ 0 & 1 & 0 \\ 0 & 0 & 1 \end{bmatrix}. \tag{23}$$

This volume scattering model can be derived from the eigenspace of the coherency matrix [39]. Contrast to $\boldsymbol{T}_{v1}$, $\boldsymbol{T}_{v4}$ usually occurs in the totally random targets. The cross polarized term T_{33} in T_{v4} is one third of the total power span (span=$T_{11}+T_{22}+T_{33}$), while T_{33} in $\boldsymbol{T}_{v4}$ is one fourth of the span, and the cross polarized term T_{33} only exists in the volume scattering models, thus the volume scattering power m_v is only decided by T_{33}, i.e., $m_v = 4T_{33}$ with $\boldsymbol{T}_{v1}$ and $m_v = 3T_{33}$ with $\boldsymbol{T}_{v4}$. The total power is fixed, the smaller volume scattering power will derive less negative surface scattering powers and double-bounce scattering powers.

The volume scattering derived from the homogeneous targets, such as vegetation areas or very rough surfaces, can be modeled by the above four available coherency matrix primly. However, for the heterogeneous targets, such as city blocks or villages, consisting of various man-made structures, the coherency matrix for volume scattering can be expressed as follows:

$$\boldsymbol{T}_{v5} = \frac{1}{15}\begin{bmatrix} 0 & 0 & 0 \\ 0 & 7 & 0 \\ 0 & 0 & 8 \end{bmatrix}. \tag{24}$$

According to [37,38], the general form of the volume scattering model is defined as (25), and the scattering powers obtained by the Freeman/eigenvalue decomposition after two rotations of the coherency matrix can be solved as (26).

$$\boldsymbol{T}_v = \begin{bmatrix} F_{11} & F_{12} & 0 \\ F_{12} & F_{22} & 0 \\ 0 & 0 & F_{33} \end{bmatrix} \tag{25}$$

$$\begin{gathered}
\text{s.t.} \quad F_{11} + F_{22} + F_{33} = 1 \\
m_v = \frac{1}{F_{33}} T_{33}(\varphi) \\
m_{d,s} = \pm\frac{\sqrt{\Delta}}{2} + \\
\frac{1}{2}\left(T_{11}(\varphi) + T_{22}(\varphi) - \frac{(F_{11}+F_{22})}{F_{33}} T_{33}(\varphi)\right) \\
\Delta = 4\left|T_{12}(\varphi) - \frac{F_{12}}{F_{33}} T_{33}(\varphi)\right|^2 + \\
\left(T_{11}(\varphi) + T_{22}(\varphi) - \frac{(F_{11}+F_{22})}{F_{33}} T_{33}(\varphi)\right)^2
\end{gathered} \tag{26}$$

3. Proposed Freeman/eigenvalue decomposition

How to select the suitable volume scattering model from the five available models (in (18), (20), (22), (23), (24)) is a key issue. Whether the target is homogeneous or heterogeneous should be determined firstly. In the coherency matrix, the diagonal terms T_{11}, T_{22} and T_{33} contain the total power and most of the physical information of the target are shown in Table 1.

Table 1 Physical meaning of the diagonal terms in $\boldsymbol{T}$

Diagonal terms	Physical meaning
T_{11}	Target symmetry
T_{22}	Target non-symmetry
T_{33}	Target irregularity

The heterogeneous targets in one resolution cell usually contain different materials, such as villages or city blocks. Targets with different materials will give more non-symmetry components in the coherency matrix than the homogeneous targets, in other words, T_{22} should be much bigger than T_{11}, i.e., $T_{22} >> T_{11}$. However, the heterogeneous targets mostly contain a nonnegligible surface scattering component, such as in the city blocks, thus the surface scattering from the streets and the double-bounce scattering from the ground-wall structure exist together in one resolution cell. Because T_{22} also exists in the surface scattering model (in (16)) and $|\alpha| < 1$, thus $T_{22} < T_{11}$ in the surface scattering model. In addition, for the volume component, it can be seen that $T_{22} \approx T_{33}$ as shown in (24). To sum up, $T_{22} > (T_{11} + T_{33})$ holds for the heterogeneous targets. For the homogeneous targets, such as the sea areas or the rough bare soil areas, the non-symmetry component or the irregularity component always has a smaller proportion in the total power, thus $T_{11} > (T_{22} + T_{33})$ can be used to represent in this case.

$$\text{Condition 1} : T_{22} > (T_{11} + T_{33}) \tag{27}$$

$$\text{Condition 2} : T_{11} > (T_{22} + T_{33}) \tag{28}$$

According to different co-polarized ratios ($R = 10\log_{10}(|S_{VV}|^2/|S_{HH}|^2)$) [18], three available volume scattering models are used. If -2 dB $< R <$ 2 dB, the target can be modeled by a cloud of the oriented thin dipole, and the volume scattering model is defined in (18). If $R < -2$ dB, the target can be modeled as a cloud of the horizontal dipole, and the volume scattering model is defined in (20). If $R > 2$ dB, the target can be modeled as a cloud of the vertical dipole, and the volume scattering model is defined in (22).

The procedure of the proposed Freeman/eigenvalue involves the following steps:

Step 1 Remove the noise of fully PolSAR data by using a sigma filter [40] with sigma=0.9, window of target=3, window of filter=9.

Step 2 Calculate the orientation angles and the OAC.

Step 3 Use the two conditions in (27) and (28) to select the volume scattering model. If Condition 1 holds, the volume scattering model is (24). If Condition 2 holds, the volume scattering model is one of (18), (20) and (22). If neither of the two conditions holds, the volume scattering model is (23). In the second case, the co-polarized ratio is used to determine the right volume scattering model.

Step 4 Decompose the coherency matrix by using (25) and (26).

4. Experiment results

To show the good efficency of the proposed Freeman/eigenvalue decomposition, several experiments are conducted on fully PolSAR data. The basic information of the data set is shown in Table 2.

Table 2 Characteristics of used data set

Sensor	Band	Looks	Resolution/m	Incidence angle/(°)
AIRSAR	L	4	10 × 10	5 – 60

The AIRSAR data set of San Francisco is downloaded from https://earth.esa.int/web/polsarpro/data-sources/sample-datasets. The original image is 900 × 1 024 pixels and shown in Fig. 1, with diagonal terms of the coherency matrix T_{11} for blue, T_{22} for red, and T_{33} green, respectively. Before composition of the RGB color image, the logarithm to base 10 and normalization are conducted on T_{11}, T_{22} and T_{33}. The zones labeled with red rectangles are used in the following tests. For convenience, the three selected zones are called Zone 1, Zone 2 and Zone 3 from top to bottom in Fig. 2. It shows the real terrains, Zone 1 is the ocean area, Zone 2 is the city block and Zone 3 is the vegetation area. The sizes of Zone 1, Zone 2 and Zone 3 are 50 × 80 pixels, 60 × 50 pixels and 60 × 50 pixels, respectively.

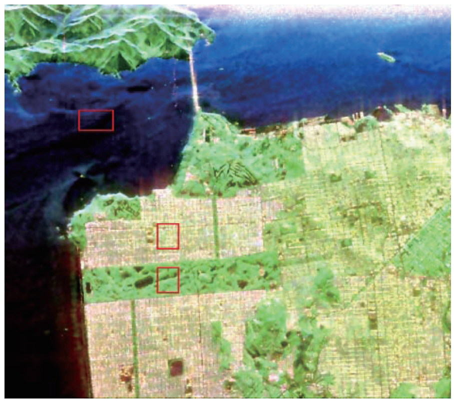

Fig. 1 AIRSAR image of San Francisco

Before the decomposition of the coherency matrix, in order to test the two conditions in (27) and (28) firstly, the pixels satisfied the conditions in the selected zones are shown in Table 3. According to the definitions in (27) and (28), Zone 1 is the ocean area, and its pixels should satisfy Condition 2 (C2). Zone 2 is the city block, and its pixels should satisfy Condition 1 (C1). In addition, because Zone 3 is the vegetation area, thus the two conditions should both not hold on it. In Table 3, 100% pixels in Zone 1 satisfy C2, and 78.48% pixels in Zone 2 satisfy C1, and 96.5% pixels in Zone 3 do not satisfy the two conditions. The results in Table 3 prove the efficiency of the proposed conditions.

Table 3 Two conditions in the selected zones

Zone	Size/pixels	C1/pixels	C2/pixels	Percentage/%
Zone 1	4 000	—	4 000	100
Zone 2	3 000	2 348	—	78.48
Zone 3	3 000	1	104	3.5

In order to illustrate the results of the proposed decomposition, four decomposition algorithms are selected to be compared. They are FDD1 [16], FDD with the coherency matrix rotation (FDD2), Freeman/eigenvalue decomposition (HFED1) [37], and Freeman/eigenvalue decomposition based on the extended volumes scattering model (HFED2) [38], respectively. The results of the decomposition of AIRSAR data are shown in Fig. 2. The surface scattering power, the double-bounce scattering power and the volume scattering power are used as the components of R, G and B in the color composite image, respectively. The proposed Freeman/eigenvalue decomposition (PD) result is shown in Fig. 2(e).

(a) FDD1

(b) FDD2

(c) HFED1

(d) HFED2

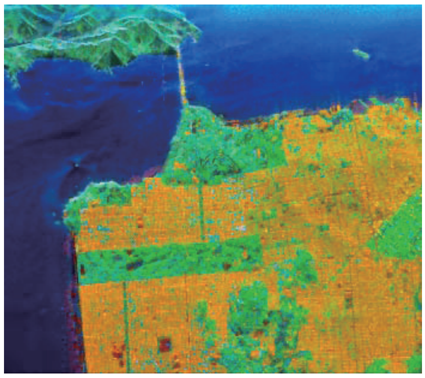

(e) PD

Fig. 2 Decomposition results of AIRSAR data

It can be observed from Fig. 2(a) to Fig. 2(e) that the scattering powers of the five decompositions can show the main terrains of the original data. Specially, the urban areas in Fig. 2(d) and Fig. 2(e) exhibit orange and pink, while the urban areas in the other methods exhibit green (FDD1) and white (FDD2 and HFED1) (double-bounce scattering m_d is the red channel).

In order to better compare the effect of the five decompositions, three small regions are selected for testing in Fig. 1. The true terrain types are the ocean area, city block and forest area, thus the dominant scattering powers of those three zones are surface scattering power m_s, double-bounce scattering power m_d and volume scattering power m_v, respectively. For convenience, all mean values are normalized by the total power of the coherency matrix. The definitions of normalized scattering powers are shown as follows:

$$\begin{cases} p_s = \dfrac{m_s}{T_{11}+T_{22}+T_{33}} \\ p_d = \dfrac{m_d}{T_{11}+T_{22}+T_{33}} \\ p_v = \dfrac{m_v}{T_{11}+T_{22}+T_{33}} \end{cases}. \tag{29}$$

The average scattering powers (average surface scattering power $\mathrm{mean\_}p_s$, average double-bounce scattering power $\mathrm{mean\_}p_d$, and average volume scattering power $\mathrm{mean\_}p_v$) in Zone 1, Zone 2, and Zone 3 are listed in Table 4, Table 5, and Table 6, respectively.

In Table 4, the five decompositions show well in Zone 1. The average scattering power $\mathrm{mean\_}p_s$ of the five decompositions are all more than 0.8. HFED1 obtains the $\mathrm{mean\_}p_s$ as 0.872, and the proposed decomposition gives the largest dominant scattering power as 0.929. The true terrain type of Zone 2 is the city block, and its structure is very complicated. The average double-bounce scattering power $\mathrm{mean\_}p_d$ of the proposed method is 0.765, which is the largest one among these methods with the values for the other four decompositions as 0.389, 0.277, 0.280, and 0.268, respectively. In Zone 3, the mean volume scattering power mean_p_v is 0.866, which is higher than the other four decompositions 0.103, 0.051, 0.047 and 0.070, respectively.

Table 4 Average scattering powers in Zone 1

Method	mean_p_s	mean_p_d	mean_p_v
FDD1	0.904	0	0.095
FDD2	0.906	0	0.093
HFED1	0.872	0.043	0.085
HFED2	0.872	0.043	0.085
PD	0.929	0	0.070

Table 5 Average scattering powers in Zone 2

Method	mean_p_s	mean_p_d	mean_p_v
FDD1	0.059	0.367	0.579
FDD2	0.138	0.488	0.375
HFED1	0.140	0.485	0.375
HFED2	0.312	0.497	0.186
PD	0.037	0.765	0.220

Table 6 Average scattering powers in Zone 3

Method	mean_p_s	mean_p_d	mean_p_v
FDD1	0.072	0.175	0.763
FDD2	0.025	0.163	0.815
HFED1	0.087	0.093	0.819
HFED2	0.109	0.093	0.796
PD	0.115	0.023	0.866

We also use the cross entropy to compare the five decompositions. The definition of the cross entropy on scattering powers is shown as follows:

$$H_p = -p_s \log_3 p_s - p_d \log_3 p_d - p_v \log_3 p_v. \qquad (30)$$

The normalized scattering powers are shown in (29). The larger domain scattering power should turn out a smaller cross entropy. The cross entropy of the five decompositions is shown in Fig. 3. The blue line, red line and green line stand for the cross entropy in Zone 1, Zone 2 and Zone 3, respectively. These methods all turn out good performance with the best one given by the PD. In addition, the cross entropy of the PD is smaller than 0.5 while the other four methods are over 0.7.

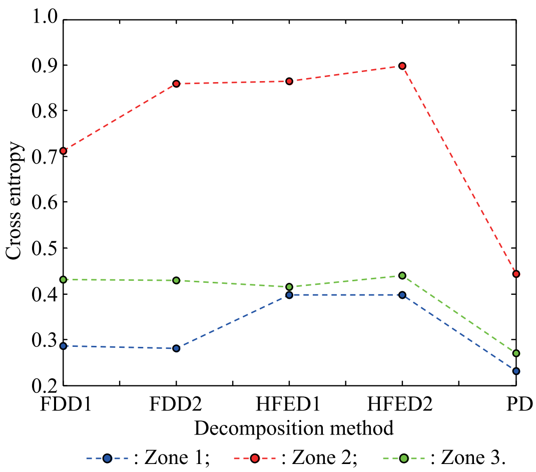

Fig. 3 Cross entropy of scattering powers

5. Conclusions

Experiments on the real PolSAR data demonstrate the effectiveness of the proposed algorithm, which improves the dominant scattering power of different terrains. The algorithm is consist of three steps, and their calculation complexity is all $O(n)$, where n is the number of the pixels, thus the calculation complexity of the proposed three-component model-based decomposition is $O(n)$. This algorithm is applied to the coherency matrix of the PolSAR data, thus the data should be multi-look. If the data are single-look, before decomposition, the data should be local averaged in a window.

References

[1] LEE J S, POTTIER E. Polarimetric radar imaging-from basics to applications. Boca Raton: CRC Press, 2008.

[2] CLOUDE R, POTTIER E. A review of target decomposition theorems in radar polarimetry. IEEE Trans. on Geoscience and Remote Sensing, 1996, 34(2): 498 – 518.

[3] YAMAGUCHI Y. Disaster monitoring by fully polarimetric SAR data acquired with ALOS-PALSAR. Proceedings of the IEEE, 2012, 100(10): 2851 – 2860.

[4] CHEN S W, WANG X S, XIAO S P. Urban damage level mapping based on co-polarization coherence pattern using multitemporal polarimetric SAR data. IEEE Journal of Selected Topics in Applied Earth Observations and Remote Sensing, 2018, 11(8): 2657 – 2667.

[5] JI Y Q, SUMANTYO S T S, CHUA M Y, et al. Earthquake/Tsunami damage assessment for urban areas using post-event PolSAR data. Remote Sensing, 2018, 10(7): 1 – 21.

[6] GUO J, WEI P L, LIU J, et al. Crop classification based on differential characteristics of H/α scattering parameters for multitemporal quad- and dual-polarization SAR images. IEEE Trans. on Geoscience and Remote Sensing, 2018, 56(10): 6111 – 6123.

[7] CHEN S W, TAO C S. PolSAR image classification using polarimetric-feature-driven deep convolutional neural network. IEEE Geoscience and Remote Sensing Letters, 2018, 15(4): 627 – 631.

[8] ZOU Y, ZHANG S L, LIANG C, et al. Research on detection oil spill information based on polarization decomposition. Proc. of the IEEE International Geoscience and Remote Sensing Symposium, 2018: 1206 – 1209.

[9] QIN X X, HU T, YU W S, et al. Edge detection of PolSAR images using statistical distance between automatically refined samples. Proc. of the IEEE International Geoscience and Remote Sensing Symposium, 2018: 645 – 648.

[10] SUO Z Y, LI M. Robust PolInSAR optimal interferogram estimation method based on generalized scattering vector. Journal of Systems Engineering and Electronics, 2017, 28(3): 457 – 471.

[11] HE W, XING M D. Classification method for PolSAR images based on find of density peak. Systems Engineering and Electronics, 2016, 38(1): 60 – 63. (in Chinese)

[12] DONALD K A, LEATITIA T L. Polarimetric phase and implications for urban classification. IEEE Trans. on Geoscience and Remote Sensing, 2018, 56(3): 1278 – 1289.

[13] BUONO A, NUNZIATA, MIGLIACCIO, et al. Classification of the Yellow River delta area using fully polarimetric SAR measurements. International Journal of Remote Sensing, 2017, 38(23): 6714 – 6734.

[14] CHEN B, WANG S, JIAO L C, et al. A three-component Fisher-based feature weighting method for supervised PolSAR image classification. IEEE Geoscience and Remote Sensing Letters, 2015, 12(4): 731 – 735.
[15] ZHANG S, WANG S, CHEN B, et al. Classification method for fully PolSAR data based on three novel parameters. IEEE Geoscience and Remote Sensing Letters, 2014, 11(1): 39 – 43.
[16] FREEMAN A, DURDEN S L. A three-component scattering model for polarimetric SAR data. IEEE Trans. on Geoscience and Remote Sensing, 1998, 36(3): 963 – 973.
[17] CLOUDE S R, POTTIER E. An entropy based classification scheme for land applications of polarimetric SAR. IEEE Trans. on Geoscience and Remote Sensing, 1997, 35(1): 68 – 78.
[18] YAMAGUCHI Y, MORIYAMA T, ISHIDO M Y, et al. Four-component scattering model for polarimetric SAR image decomposition. IEEE Trans. on Geoscience and Remote Sensing, 2005, 43(8): 1699 – 1706.
[19] FREEMAN A. Fitting a two-component scattering model to polarimetric SAR data from forests. IEEE Trans. on Geoscience and Remote Sensing, 2007, 45(8): 2583 – 2592.
[20] ARII M, ZYL J J, KIM Y J. Adaptive model-based decomposition of polarimetric SAR covariance matrices. IEEE Trans. on Geoscience and Remote Sensing, 2011, 49(3): 1104 – 1113.
[21] ANTROPOV O, RAUSTE Y, HAME T. Volume scattering modeling in PolSAR decomposition: study of ALOS PALSAR data over Boreal forest. IEEE Trans. on Geoscience and Remote Sensing, 2011, 49(10): 3838 – 3848.
[22] WANG Z Z, ZENG Q M, JIAO J. A new volume scattering model for three-component decomposition of polarimetric SAR data. Proc. of the IEEE International Geoscience and Remote Sensing Symposium, 2018: 4575 – 4578.
[23] XIE Q, BERMAN J D B, SANCHEZ J M L, et al. On the use of generalized volume scattering models for the improvement of general polarimetric model-based decomposition. Remote Sensing, 2017, 9(2): 117.
[24] WANG X, ZHANG L M, ZHU S. A four-component decomposition model for polarimetric SAR images based on adaptive volume scattering model. Proc. of the IEEE International Geoscience and Remote Sensing Symposium, 2018: 4563 – 4566.
[25] XIE Q H, ZHU J J, SANCHEZ J M L, et al. A modified general polarimetric model-based decomposition method with the simplified Neumann volume scattering model. IEEE Geoscience and Remote Sensing Letters, 2018, 15(8): 1229 – 1233.
[26] DUAN D F, WANG Y. An improved algorithm to delineate urban targets with model-based decomposition of PolSAR data. Remote Sensing, 2017, 9(10): 1037 – 1054.
[27] XI Y Y, LANG H T, TAO Y H, et al. Four-component model-based decomposition for ship targets using PolSAR data. Remote Sensing 2017, 9(10): 621 – 639.
[28] HUANG X, WANG J, SHANG J. An integrated surface parameter inversion scheme over agricultural fields at early growing stages by means of C-band polarimetric RADARSAT-2 imagery. IEEE Trans. on Geoscience and Remote Sensing, 2016, 54(5): 2510 – 2528.
[28] LIM Y X, BURGIN M S, ZYL J J V. An optimal nonnegative eigenvalue decomposition for the Freeman and Durden three-component scattering model. IEEE Trans. on Geoscience and Remote Sensing, 2017, 55(4): 2167 – 2176.
[30] XIANG D, WANG W, TANG T, et al. Multiple-component polarimetric decomposition with new volume scattering models for PolSAR urban areas. IET Radar, Sonar and Navigation, 2017, 11(3): 410 – 419.
[31] SINGH G, YAMAGUCHI Y. Model-based six-component scattering matrix power decomposition. IEEE Trans. on Geoscience and Remote Sensing, 2018, 56(10): 5687 – 5704.
[32] XU F, JIN Y Q. Deorientation theory of polarimetric scattering targets and application to terrain surface classification. IEEE Trans. on Geoscience and Remote Sensing, 2005, 43(10): 2351 – 2364.
[33] CHENG S W, WANG X S, XIAO S P, et al. Target scattering mechanism in polarimetric synthetic aperture radar. Singapore: Springer, 2018.
[34] LEE J S, ANISWORTH T. The effect of orientation angle compensation on coherency matrix and polarimetric target decompositions. IEEE Trans. on Geoscience and Remote Sensing, 2011, 49(1): 53 – 64.
[35] AN W, CUI Y, YANG J. Three-component model-based decomposition for polarimetric SAR data. IEEE Trans. on Geoscience and Remote Sensing, 2010, 48(6): 2732 – 2739.
[36] SINGH G, YAMAGUCHI Y, PARK S E. General four-component scattering power decomposition with unitary transformation of coherency matrix. IEEE Trans. on Geoscience and Remote Sensing, 2013, 51(5): 3014 – 3022.
[37] CLOUDE S R. Polarisation: applications in remote sensing. London: Oxford University Press, 2009.
[38] SINGH G, YAMAGUCHI Y, PARK S E. Hybrid Freeman/eigenvalue decomposition method with extended volume scattering model. IEEE Geoscience Remote Sensing Letters, 2013, 10(1): 81 – 85.
[39] ZHANG S, WANG S, JIAO L C. A novel hybrid Freeman/eigenvalue decomposition with general scattering models. Journal of Infrared and Millimeter Waves, 2015, 34(3): 265 – 270.
[40] LEE J S. Improved sigma filter for speckle filtering of SAR imagery. IEEE Trans. on Geoscience and Remote Sensing, 2009, 47(1): 202 – 213.

Biographies

ZHANG Shuang was born in 1983. She received her B.S. degree in School of Information Engineering from Liaoning University in 2006, Shenyang, China. She received her Ph.D. degree in School of Electronic Engineering from Xidian University, Xi'an, China, in 2015. She is currently a lecturer at School of Automation and Information Engineering, Xi'an University of Technology, Xi'an, China. Her research interests are interpretation and processing of PolSAR data and deep learning in the complicated data.
E-mail: zhangshuang@xaut.edu.cn

YU Xiangchuan was born in 1984. He received his B. S. and M.S. degrees in School of Electronic Engineering from Xi'an University in 2006 and 2009 respectively, Xi'an, China. Now, he is an engineer in Caltta Technologies Co., Ltd. His main research interests are private network communication and image processing.
E-mail: yu.xiangchuan@zte.com.cn

WANG Lu was born in 1986. She received her B.S. degree in School of Electronic Engineering from Xi'an University of Posts and Telecommunications, Xi'an, China, in 2008, and her Ph.D. degree in School of Electronic Engineering from Xidian University, Xi'an, China, in 2014. She is currently a lecture at School of Automation and Information Engineering, Xi'an University of Technology, Xi'an, China. Her research interests are X-ray pulsar navigation and weak radar signal processing.
E-mail: wanglu_xidain@163.com